Published in final edited form as:
J Phys Chem C Nanomater Interfaces. 2012 November 15; 116(45): 24380–24389. doi:10.1021/jp309053z.

Citrate-capped gold nanoparticle electrophoretic heat production in response to a time-varying radiofrequency electric-field

Stuart J. Corr[1,2,3], **Mustafa Raoof**[1], **Yuri Mackeyev**[2], **Sophia Phounsavath**[1,2], **Matthew A. Cheney**[1,2], **Brandon T. Cisneros**[1], **Michael Shur**[4], **Michael Gozin**[4], **Patrick J. McNally**[3], **Lon J. Wilson**[2], and **Steven A. Curley**[1,5,*]

[1]Department of Surgical Oncology, University of Texas M. D. Anderson Cancer Center, Houston, TX 77030, USA. [2]Department of Chemistry and The Richard E. Smalley Institute for Nanoscale Science and Technology, Rice University, Houston, TX 77005, USA. [3]Nanomaterials Processing Laboratory, The Rince Institute, Dublin City University, Dublin 9, Rep. of Ireland. [4]School of Chemistry, Beverly and Raymond Sackler Faculty of Exact Sciences, Tel Aviv University, Tel Aviv 69978, Israel. [5]Mechanical Engineering and Materials Science, Rice University, Houston, TX 77005, USA.

Abstract

The evaluation of heat production from gold nanoparticles (AuNPs) irradiated with radiofrequency (RF) energy has been problematic due to Joule heating of their background ionic buffer suspensions. Insights into the physical heating mechanism of nanomaterials under RF excitations must be obtained if they are to have applications in fields such as nanoparticle-targeted hyperthermia for cancer therapy. By developing a purification protocol which allows for highly-stable and concentrated solutions of citrate-capped AuNPs to be suspended in high-resistivity water, we show herein, for the first time, that heat production is only evident for AuNPs of diameters ≤ 10 nm, indicating a unique size-dependent heating behavior not previously observed. Heat production has also shown to be linearly dependent on both AuNP concentration and total surface area, and severely attenuated upon AuNP aggregation. These relationships have been further validated using permittivity analysis across a frequency range of 10 MHz to 3 GHz, as well as static conductivity measurements. Theoretical evaluations suggest that the heating mechanism can be modeled by the electrophoretic oscillation of charged AuNPs across finite length scales in response to a time-varying electric field. It is anticipated these results will assist future development of nanoparticle-assisted heat production by RF fields for applications such as targeted cancer hyperthermia.

Keywords

Radiofrequency; Gold; Nanoparticles; Heating; Permittivity

*Corresponding author: Anderson Cancer Center, Division of Surgery, Unit 1447, 1400 Pressler St, Houston, TX 77230-1402, Phone: 713-794-4957, Fax: 713-745-2436. .
Stuart J. Corr: SJCorr@mdanderson.org, **Mustafa Raoof**: MRaoof@mdanderson.org, **Yuri Mackeyev**: mackeyev@rice.edu, **Sophia Phounsavath**: sp3@rice.edu, **Matthew A. Cheney**: mac5@rice.edu, **Brandon T. Cisneros**: BTCisneros@mdanderson.org, **Michael Shur**: shur.michael@gmail.com, **Michael Gozin**: cogozin@mgchem.tau.ac.il, **Patrick J. McNally**: patrick.mcnally@dcu.ie, **Lon J. Wilson**: durango@rice.edu, **Steven A. Curley**: scurley@mdanderson.org.

Supporting Information Available: Supporting information (as referred to in the texts as Figures S1 to S11) can be found free of charge via the Internet at http://pubs.acs.org.

1. INTRODUCTION

The size-dependent optical, magnetic and electrical properties of various nanoparticle (NP) materials are currently being exploited for cancer therapy based on hyperthermia-initiated cellular necrosis.[1] These emerging cancer-heating nanotechnologies potentially permit targeted, cell–specific oncologic approaches which could be complimentary and possibly superior to current cancer treatments such as proton-, chemo-, radiation- and immuno-therapy, as well as surgical resection. For example, by utilizing photo-thermal heat production of AuNPs irradiated with UV-Vis/NIR optical energy,[1a] cancer cells can effectively be ablated from the "inside-out".

An alternative, but related, line-of-thought for expanding NP-mediated cancer therapy is based on the interaction of RF energy with nanomaterials such as AuNPs. It has been hypothesized that such heat-inducing interactions could initiate targeted hyperthermia or thermal ablation within cancer cells. Although it has been previously shown that AuNPs and carbon nanotubes promoted *in vitro* and *in vivo* RF thermal ablation of hepatocellular, colorectal, and pancreatic cancer,[2] recent work has concluded that the AuNP heating effects (in non-biological systems) originate from Joule heating of the ionic buffer suspensions and not Joule heating within the NPs themselves, as was suggested in our previous work.[3] In particular, some work has experimentally and theoretically questioned the validity of physical heat production from RF interaction with AuNPs.[4]

Herein we show that spherical citrate-capped AuNPs suspended in ultra-pure, buffer(ion)-free water generate heat in a concentration-dependent manner. More intriguingly, for the range of NP diameters investigated (5 nm to 50 nm), heat production was only evident for the sub-10 nm diameters which has led us to coin the term "ultra-small gold nanoparticles" (US-AuNPs) to differentiate between RF-active and RF non-active AuNPs. The results of our studies demonstrate that the heating mechanism is strictly dependent on the US-AuNP concentration and surface area (including the citrate coating concentration) and that heat production is significantly attenuated when the US-AuNPs are aggregated.

The heat response was evaluated using an RF system with a thermal imaging camera. Electrical characterization of the AuNP samples was also performed via liquid permittivity and conductivity measurements. Taken together, these results confirm a size-, concentration- and surface-area-dependent relationship for US-AuNP heat production under RF excitation. Also, using both experimental probe methods and computer simulations we have been able to evaluate the electric field intensity in-and-around our samples which was shown to be ~90 kV/m in air and between 0.63 kV/m - 2.3 kV/m across the sample itself.

Although these experimental results warrant a more rigorous theoretical evaluation (outside the scope of this article), we speculate that the heating mechanism can be modeled via the electrophoretic oscillation of charged particles within a liquid medium in response to a time-varying electric field in accordance with recent theoretical work by Sassaroli *et al.*[5]

2. EXPERIMENTAL SECTION

2.1 Sample preparation and analysis

Citrate-stabilized AuNPs of average diameters 5, 10, 20, and 50 nm were purchased from Ted Pella Inc. and shown to be monodispersed, nearly spherical, with a size dispersion similar to that stated by the manufacturer, as determined by TEM imaging. The AuNPs came suspended in 500 ml of buffer solution that contained unspecified quantities of ions from citric acid, tannic acid, and potassium carbonate, all of which have been rigorously removed in order to eliminate background Joule heating by the RF field. This was achieved

by brief centrifugation at low-peed (3,500 rpm and 125 s, respectively) through a 50 kDa centrifuge filter which allowed approximately 70 % of the buffer to pass through the filter pores, leaving behind the AuNPs which were then resuspended in high-resistivity water (Ω-water, 18.2 MΩ/cm). This process, as highlighted in Figure 1, was repeated eight times until the RF heating rates (HRs) of the removed diluted buffers were identical to that of the Ω-water, indicating complete removal of buffer salt contaminants.

Elimination of trace levels of buffer contaminants was also verified by monitoring UV-Vis absorption spectra (Supporting Information S1) using a quartz cuvette scanning from 284 nm to 1134 nm (Applied Nanofluorescence, Houston, TX, USA), as well as inductively-coupled plasma optical emission spectroscopy (ICP-OES, Perkin Elmer Optima 4300 DV, Waltham, MA, USA) measurements for gold to verify the absence of gold from any AuNPs that may have passed through the filter membrane (data not shown). Also, AuNP stability was investigated using the UV-Vis apparatus previously described, as well as zeta potential measurements (Malvern Zen 3600 Zetasizer, Worchester, UK) at a pH of approximately 5.2 which is equivalent to the pH of the Ω-water (slightly acidic due to absorption of CO_2). TGA analysis (Q-600 Simultaneous TGA/DSC, TA Instruments, Newcastle, DE, USA) was taken under argon atmospheric pressure across the temperature range 30 °C to 1100 °C to determine the mass percentage of surfactant and gold for both stable and aggregated AuNPs of all diameters, as well as the stock solutions.

2.2 Radiofrequency heating system

Figure 1D depicts the Kanzius RF system which includes modifications designed by ThermMed, LLC, Inc. (Erie, PA, USA) and include an internal RF-coil cooling apparatus connected to external chillers to prevent heat generation from the coils influencing the sample HRs (because of this, the power wattage quoted for previous systems[2-3, 6] should not be compared to the current system). In brief, samples were placed in a 1.3 ml quartz cuvette held by a custom-designed Teflon holder mounted to an adjustable rotary stage under open air conditions at ambient room temperature as described previously.[2-3] The cuvette was placed 0.8 cm from the transmission head of the RF-field generator located at an arbitrary point on the X-Y plane (7.6 cm, 10.2 cm) with a 8 cm air gap between transmitting and receiving heads. The solutions were then exposed to the high-voltage RF fields (~90 kV/m, as discussed below) at 950 W generator power (13.56 MHz operating frequency). Temperatures were recorded every 0.1625 seconds with an infrared camera (FLIR SC 6000, FLIR Systems, Inc., Boston, MA, USA) for a duration of 120 s or until the sample reached 70 °C (higher temperatures were not attempted to prevent electrical arcing due to excess water evaporation). The temperature of four control areas were also recorded to subtract any stray heating effects from the instrument and/or Teflon holder (Figure 1E). All samples were exposed to the RF instrument once these four control areas had similar temperatures. HRs were calculated along the linear portion of the heating curve since no exponential component could be seen such as that arising from the steady-state rate of heat flow (Supporting Information S2).

The first part of the experiment involved exposing the stock AuNP solutions, as well as their extracted buffers (as a function of wash number), to the RF system. Secondly, purified AuNPs of concentrations 250, 500, 1000, and 2000 mg/L dispersed in Ω-water were first exposed to the RF system and then centrifuged through a 50 kDa filter to remove the Ω-water; the filtrate was then re-exposed to the RF-field. The difference in HRs between these two solutions determined heat production due to the presence of the AuNPs (including their citrate coating and counter-ions). This process was repeated five times for each sample with a minimum of three experimental runs from at least two different stock solutions (of similar-sized AuNPs)

2.3 Electrical characterization

Electrical characterization such as permittivity (frequency-dependent) and static solution conductivity (D.C.) analysis can help predict how an RF-field system will interact with various materials and solutions. Complex permittivity measurements were taken using an Agilent 85070E high-temperature coaxial dielectric probe (Agilent Technologies, Santa Clara, CA, USA) connected to an Agilent E4991A impedance analyzer across the frequency range 10 MHz to 3 GHz (similar to the procedure used by Gach *et al.*[7]). Approximately 800 logarithmic data points were taken across the specified frequency range with each measurement taken 10 times. This procedure was repeated three times. Static solution D.C. conductivity analysis was taken using an InLab®741 ISM Conductivity Probe (Mettler Toledo, Columbus, OH, USA) connected to a SevenCompact™ conductivity S230 bench meter (Mettler Toledo, Columbus, OH, USA). Each sample was analyzed five times. This procedure was also repeated three times.

3. RESULTS AND DISCUSSION

3.1 RF heating data of stock AuNP solutions

Figure 2 depicts the HRs for all the stock AuNP samples, as well as their removed and diluted buffers. The HRs for the stock solutions are identical to their extracted buffers, indicating that the buffers are a major source of heat production due to Joule heating. Similar buffer heating characteristics were observed by Li *et al.*[4b] who attributed AuNP HRs to the buffer suspensions and not the AuNPs themselves. These findings must be taken into account when analyzing previous RF experiments that suggested a size-dependent Joule heating mechanism of AuNPs, as stated by Moran *et al.*[3] Figure 1 also shows that at least eight buffer washes are needed before the HRs are equal to Ω-water (0.01 °C/s). Any heat production from the AuNPs resuspended in Ω-water after eight buffer washings is due to the AuNPs themselves and not the buffer media. Also, stock solution HRs for all AuNPs were linearly proportional to exposed RF power (Figure 2B) with values similar to those reported by both Kruse *et al.* [8] and Li *et al.*[4b] who used similar systems but at much lower powers (and thus, much lower electric field strength).

3.2 RF heating data for purified AuNP suspensions

Figure 3 depicts the individual experimental data for each AuNP diameter. Each sample and corresponding filtrate was exposed to the RF field five times. Each experiment was repeated 7, 6, 5, and 4 times for 5, 10, 20, and 50 nm AuNPs, respectively, using three sample bottles of stock AuNPs for 5 and 10 nm, and two sample bottles for 20 and 50 nm AuNPs. Figure 4A depicts the *concentration*- and *size-dependent* HRs for the 5 nm and 10 nm diameter US-AuNPs. No heat was observed for AuNPs of diameters 20 nm and 50 nm (see Supporting Information S3-S5 for extra data including TEM images of purified AuNPs). Figure 4B expresses the data in Figure 4A as a function of total US-AuNP surface-area in each 1.3 ml sample (calculated using the standard mass, density, and volume relationship and assuming spherical morphology). For example, a 2000 mg/L sample suspension of 10 nm AuNPs has approximately the same total surface area (~0.05 m^2) and HR as a 1000 mg/L suspension of 5 nm AuNPs, per 1.3 ml sample volume. This surface-area relationship suggests that, on a per-NP-basis, a 10 nm US-AuNP would generate four times as much heat as a 5 nm US-AuNP (due to R^2 dependency).

Only by creating highly-concentrated and buffer(ion)-free suspensions of AuNPs with diameters less than 10 nm could the heating nature of AuNPs in response to an RF electric-field be observed and analyzed in our experiments. Furthermore, these are most likely the reasons why heating effects have not been observed in previous experimental

investigations[4b, 8-9] as these experiments either used low power RF systems, low concentrations, or AuNPs with diameters > 10 nm.

3.3 AuNP suspension stability analysis

Figure 5A illustrates AuNP plasmon peak positions for the stock, washed, and RF-exposed AuNPs (see Supporting Information S6 for full spectrum). For 5 nm US-AuNPs, we attribute the initial 3.6 nm peak shift due to the change in the external dielectric constant of the suspension medium after removal of the yellow buffers since plasmon resonance is a direct function of the AuNP internal and external dielectric constants. For 20 nm AuNPs, we hypothesize that the initial peak shifts are due to the removal of ions and salts from the aqueous solution that previously would have resided on the NP surface through citrate-ionic interactions which would effectively create an excess of ions around the AuNPs. In some cases, slight peak-shifts after RF-exposure were due to partial removal of residual surface surfactant from the NP surface caused by filter centrifugation for the Ω-water analysis (see Supporting Information S4 for UV-Vis evidence of residual buffer).

The zeta potential measurements in Figure 5B show that 5 nm and 10 nm US-AuNPs increase their negative surface charge after buffer removal. Similar to UV-Vis interpretations, we assume that this is due to the removal of excess buffer counter-ions, which otherwise would be interacting with the AuNP citrate-coating, effectively increasing the AuNP mass and reducing the electrophoretic mobility which, in turn, directly affects the zeta potential. The slight decrease in charge after RF exposure is again, as previously mentioned, due to slight aggregation of the AuNP suspension from further loss of surface surfactant after centrifugation to remove the Ω-water. Zeta potential values for 20 nm and 50 nm AuNPs follow intuition in that the loss of surface surfactant from repeated centrifugation (to remove the buffers) reduced the surface charge.

3.4 RF heating effects from US-AuNP aggregation

Overall, since all samples were still suspended in the solution after one week (no precipitation) with no UV-Vis evidence of quadrupole or broadened dipolar plasmon peaks, including reasonably stable zeta potential measurements, we conclude that all the solutions contain highly-stable, non-aggregated AuNPs in Ω-water medium. Also, by inducing AuNP aggregation through excessive and high-speed centrifugation (27,000 rpm for 9 hours) the HRs for the 5 and 10 nm US-AuNPs were attenuated to just ~0.07 °C/s each (data not shown), which is approximately 6.5 and 3.0 times less than that of the non-aggregated US-AuNPs samples of the same concentration (2000 mg/L). Aggregation was confirmed by plasmon peak shifts and broadening of the UV-Vis spectrum, as well as TGA analysis (Supporting Information S7 and S8 respectively), which showed a reduction in citrate mass from ~10 % to ~2 % for the non-aggregated and aggregated AuNPs, respectively. This effect of heat attenuation, as a function of US-AuNP aggregation, compliments the recent *in vitro* work of Raoof *et al.*[10] who demonstrated that 10 nm US-AuNPs can be optimized for targeted RF cancer therapy by modulating the pH of the cellular endolysosomal environment to prevent AuNP aggregation.

3.5 Permittivity and conductivity relationships

Figure 6A depicts the permittivity loss (ε'') data for 5 nm and 10 nm US-AuNPs, as well as for 20 nm AuNPs at concentrations of 2000 mg/L, across the RF-frequency spectrum of 10 MHz - 300 MHz (see Supporting Information S9 for full spectrum up to 3 GHz). The precise values for ε'' (after subtracting the background Ω-water permittivity data) at AuNP concentrations of 2000 mg/L and 1000 mg/L are shown on the left-hand primary y-axis of Figure 6B. Direct current (D.C.) conductivity values are also shown on the right-hand secondary y-axis (see Supporting Information S10 for full data). Similar to the RF heating

studies, both the permittivity and conductivity values show a size-, concentration-, and surface area-dependent relationship for RF exposure. The conductivity values fell to negligible levels for the aggregated US-AuNPs described above (data not shown).

3.6 Dielectric loss equations to predict US-AuNP power dissipation

The ability of a material to store and dissipate electrical energy as heat can be described by the real (ε') and imaginary (ε'') parts of the complex permittivity function. This relationship is given by Equation 1:

$$\varepsilon^*(\omega) = \varepsilon'(\omega) - i\varepsilon''(\omega) \quad (1)$$

where ω is the radial frequency ($2\pi f$) . Considering that US-AuNP permittivity and conductivity measurements exhibited similar size-, concentration, and surface-dependent relationships to RF excitations, this strongly suggests that their RF heating properties can be modeled using equations that describe effective conductivity and/or complex permittivity. Equation 1 can be modified to give a direct relationship to specific absorption rate (SAR, W/kg) with respect to electric field strength (E) and permittivity (ε'')/conductivity (σ) according to Equation 2:

$$SAR = \frac{\sigma(\omega)|E|^2}{\rho} = \frac{\varepsilon^0 \omega \varepsilon''(\omega)|E|^2}{\rho} \quad (2)$$

where ε^0 is the vacuum permittivity of free-space (8.85×10^{-12} F/m), ω the radial frequency, and ρ the density (kg/m^3). This relationship can also be modified to give the theoretical increase in temperature by using Equation 3:

$$\Delta T = \frac{\varepsilon^0 \omega \varepsilon''(\omega)|E|^2 t}{2\rho C} \quad (3)$$

where C is the specific heat capacity (J/(kg.K)), and t is time (s). Although accurate values for the permittivity loss and D.C. conductivity were measured, it is also necessary that an accurate value for the E-field strength (V/m) be calculated in order to utilize these equations.

3.7 Electric-field measurements and simulations

High-power RF E-field measurements are notoriously difficult to obtain and, indeed, several limitations and obstacles surround such an endeavor. However, an attempt to measure the E-field was instigated nonetheless, using a custom-made 28 cm long E-field probe (designed by ThermMed, LLC, Inc., Erie, PA, USA) connected to an oscilloscope (a full system schematic and experimental description is given in the Supporting Information S11). Using this set-up, it was possible to accurately measure the RF voltage up to about 300 W RF-power, at which point the probe started to heat significantly. Measurements were taken up to 300 W by allowing the RF-system to operate for a maximum of 4 s, which was just enough time to take a reading without inducing destructive heating effects that would occur at ~120 °C due to the probe materials.

The magnitude of E-field strength versus power (100 W to 300 W) is shown in Figure 7. As can be seen, the E-field showed a linear power-dependent response across the measured power range. Given that the HRs of the stock AuNP solutions (Figure 2B), as well as a normal saline solution (0.9 % NaCl, Figure 8), exhibited a linear response across 100 W to 950 W, we hypothesize that the gradient of the measured E-field across 100 W to 300 W be used to calculate the E-field strength at 950 W, which would be ~90 kV/m (higher than that

stated previously[2b]). This variation is most likely due to the addition of several new cooling components into the current system which would have altered the electric field intensity.

Having measured an approximate value for the E-field in air, software simulations were performed using Coulomb 3D (INTEGRATED Engineering Software, Manitoba, Canada) to calculate the E-field in-and-around a saline solution and are highlighted in Figure 9. Both Figures 9A and 9B depict the magnitude of the E-field intensity (as contour and arrow vector plots, respectively) around an exact replica of the quartz cuvette used in our system, filled with 1.3 ml of normal saline. The permittivity values of this solution ($\varepsilon' = 76$, and $\varepsilon'' = 1989$) were taken from the previous published results by Gach *et al.*[7] using a permittivity setup identical to ours. Although Gach *et al.* evaluated a saline solution containing 0.02 % Pluronic F108, the pluronic had a negligible difference on the saline permittivity values and was omitted in our study (although we did verify the negligible difference ourselves using our permittivity setup, data not shown).

As can be seen there is a relatively uniform attenuation of the E-field across the whole z-axis of the saline sample area but there are areas of concentrated E-field intensities, such as that contained at the saline/air interface (point iv in Figure 9A and 9C) where the E-field is increased considerably, presumably due to the curvature of the sample surface and the large saline/air impedance mismatch.

In Figure 9C an E-field versus distance graph was taken across a vertical line segment which runs directly through the sample (from Z0 to Z3 in Figure 9B). The gradual increase in E-field intensity from Z0 to point (i) is due to the linear increase in E-Field strength as the distance from the Tx head to the sampling point gets smaller. The step-decrease at point (ii) is due to the E-field coming into contact with the quartz cuvette wall where it is attenuated by a factor of 3.7 (relative permittivity of quartz). The E-field in the saline sample itself displays a parabolic curve shape with a peak in the center. This is most likely due to the curved nature of the cuvette slightly focusing the E-fields into the center of the sample. Finally, there is a very large step-increase at point iv due to the saline/air interface where the E-field increases from 1.1 kV/m to 87.1 kV/m. This linear-step is increased by a factor of 79.1, which is very close to the relative permittivity of the sample ($\varepsilon' = 76$) indicating close agreement between model simulations and the E-field value measured using the probe setup. As such, the E-field in the saline sample itself can be stated to range from ~0.63 kV/m to 2.3 kV/m, with the E-field value in air being ~ 90 kV/m. These values are summarised in Table 1.

Using an E-field value of 1.1 kV/m in Equation 2 would give an SAR value of ~1811 W/kg. Also, inputting this E-field value into Equation 3 would give an average HR of ~0.21 °C/s, which is almost identical to the experimental average HR of the saline solution which was found to be 0.22 °C/s. Given that these two values are almost identical, we can now use the permittivity values of the US-AuNP solutions to compare experimental and theoretical HRs (using Equations 2 and 3).

As can be seen in Table 2, there is a large discrepancy between the experimental and theoretically derived SAR/HRs for the 5 nm and 10 nm US-AuNP solutions at 2000 mg/L. Given that the experimentally measured HRs for each of these solutions were 0.45 °C/s and 0.22 °C/s, respectively, one would expect the theoretically derived values for SAR and HR to be at least equal (for the 10 nm US-AuNPs) or larger than the values for the saline sample. The SAR values are 1.82 and 1.24 W/kg for 5 nm and 10 nm US-AuNP samples, respectively, compared to 1811 W/kg for the saline solution. Also, the HRs are 2.18×10^{-4} °C/s and 1.47×10^{-4} °C/s for 5 nm and 10 nm US-AuNP samples, respectively, compared to 0.21 °C/s for the saline solution. These results ultimately suggest that, although the classical

dielectric heat equations governed by Equations 2 and 3 can accurately be used to model the behavior of aqueous electrolyte suspensions such as saline, when it comes to US-AuNP suspensions, something more is needed.

3.8 Origins of US-AuNP heating mechanism

There have been several papers published recently which have modeled the interaction of AuNPs with low-frequency electric-fields in order to evaluate heat production. Previous models by Hanson *et al.*[4a, 11] have included Mie theory for the absorption of electromagnetic energy by metallic and dielectric NPs (with and without absorbing coatings), as well as electronic absorption occurring at the surface of the NPs due to electron spill-out, surface roughness, and effects of surface phonons.

In regards to optimizing NP design for increased RF absorption, the maximum possible cross-sectional absorption area was found to be 1.6×10^{-20} m^2 for a 200 nm diameter spherical NP of conductivity 0.078 $S.m^{-1}$ (very low when compared to 4.6×10^7 $S.m^{-1}$ for gold) and is strongly dominated by the electric dipole contribution. For AuNPs with similar diameters, with-and-without a 1 nm thick dielectric coating of conductivity 0.0063 $S.m^{-1}$, the cross-sectional absorption area was calculated to be ~2.1×10^{-21} m^2 and ~2.67×10^{-26} m^2, respectively, and is strongly dominated by the magnetic dipole contribution.

As an extension to this work, a separate theoretical thermodynamic evaluation by Hanson *et al.*[4a] was initiated which modeled a system very similar to ours that comprised of 40 nm diameter AuNPs (of volume fraction 10^{-6} with a coating of conductivity 0.01 $S.m^{-1}$) suspended in 1.5 ml of DI water (in a cuvette) under ambient open-air conditions (the value used for coating conductivity was estimated to be similar to that of citrate). Even with these parameters and using an E-field strength of ~12.5 kV/m (taken from our previous work on an older RF system) they concluded that at RF frequencies the absorption of metallic AuNPs is too small, even for unit volume fractions to enhance absorption and that any observed heating is directly due to the water itself[4a]. It was also stated that to achieve a noticeable increase in temperature by tens of degrees the power absorbed per NP would need to be increased by a factor of 10^7 which would be unlikely to happen even given the new E-field value of 90 kV/m.

Similar trends have also been published by other investigators. The most recent theoretical models by Sassaroli *et al.*[5] looked at both Mie theory and Maxwell–Wagner effective medium theory (with the effect of the counter-ion relaxation and electric-double layer taken into account), as well as dielectric loss as a function of electrophoretic particle acceleration. Similar to the results of Hanson *et al.*,[4a, 11] they demonstrated using numerical simulations that dielectric losses are primarily dominated by the host medium with negligible contribution from the AuNPs. The effect of the electric-double layer in the context of Maxwell-Wagner theory was also investigated and found to be *minimal* in enhancing the absorption properties of AuNPs (although the electric double-layer did effect the conductivity of the NP).

However, large dielectric losses were predicted when looking at RF absorption in terms of the motion of charged NPs acted upon by a time-dependent electric field. If we compare our experimental data with their numerical simulations of electrophoretic movement of charged NPs in a water medium, direct parallels can be drawn. They showed that dielectric loss was proportional to NP surface charge and concentration, yet *inversely* proportional to size (for a fixed volume fraction). In this case, the size-dependency is explained by a suspension of 5 nm diameter AuNPs having eight times more NPs than a 10 nm AuNP suspension for the same concentration (mg/L) and would contain more surface charge per unit volume.

The work by both Hanson *et al.* and Sassaroli *et al.* suggests that our experimentally observed heating rates could be due to the motion of charged US-AuNPs (over finite distances of Å length scales) in response to a time-varying electromagnetic field. In effect, the US-AuNPs would resemble large negatively-charged ions due to the action of the negatively-charged citrate-capping layer. This would also explain the size-dependent heating relationship as larger AuNPs would would appear to be more viscous within the water suspension: inhibiting the particles from achieving maximum velocity. In this regards, we attempted to evaluate and compare our experimental permittivity and heating values to the models proposed by Sassaroli *et al.*

3.9 Heat production via electrophoretic particle acceleration

Using the equations given by Sassaroli *et al.*[5] for electrophoretic particle acceleration in response to a time-varying electric field vector, the complex permittivity function $\left(\bar{\varepsilon}_{flow}=\varepsilon'_{flow}-i\varepsilon''_{flow}\right)$ in relation to a collection of flowing charged particles in a liquid medium can be broken down into imaginary and real components as shown in Equations 4a and 4b, respectively

$$\varepsilon'_{flow}=-\frac{\mathcal{N}q^2}{\beta}\frac{\tau}{1+(\omega\tau)^2} \quad (4a)$$

$$\varepsilon''_{flow}=-\frac{\mathcal{N}q^2}{\beta\omega\varepsilon_0}\frac{\tau}{1+(\omega\tau)^2} \quad (4b)$$

where $\mathcal{N}$ is the number of NPs per unit volume, q is the NP charge, β is the friction coefficient given by Stoke's law ($\beta = 6\pi\mu fa$ where μf is the coefficient of viscosity of the host medium and a is the NP radius), τ is equal to m/β (where m is the NP mass), ε_0 is the vacuum permittivity of free space, and ω is the angular frequency.

For a collection of charged metallic NPs, the number N of excess surface charge depends on the particle radius according to

$$N(a)=Aa+Ba^2 \quad (5)$$

where $A \cong 3\ nm^{-1}$ and $B \cong 0.5\ nm^{-2}$. The excess surface charge is then calculated as $q = N \times e_0$ with e_0 the charge of an electron. Using 5 nm and 10 nm US-AuNP samples at a concentration of 2000 mg/L (10.2 mM/L), which is equivalent to a volume fraction (Ø) of 1.03×10^{-4}, a plot of dielectric loss (ε'') versus frequency is shown in Figure 10. As can be seen, the dielectric loss of both 5 nm and 10 nm solutions, for N calculated by Equation 5, are similar to one another and depict a sharp exponential reduction from around 1 MHz onwards. These calculated curves are also similar to the experimental values of dielectric loss (as was shown previously in Figure 6) and are identical when the values of N are changed slightly from 25.8 to 39.5 and 101.6 to 103, for 5 nm and 10 nm US-AuNPs, respectively.

The physical parameters contained in Equation 4b can hence be used to evaluate heat production using alternative heating equations to the standard SAR equation (Equation 2). The electrophoretic current density J (Amps/m^2) and velocity v_0 of the charged NPs can be calculated as follows[5]:

$$J=\mathcal{N}qv_0e^{iwt} \quad (6a)$$

$$v_0 = \frac{qE_0}{\beta}\frac{1}{1+i\omega\tau} \quad (6b)$$

The maximum obtainable velocity (qE_0/β) of the 5 nm and 10 nm AuNPs would be 1.57×10^{-4} m/s and 2.64×10^{-4} m/s, respectively, for an E-field strength of 2.3 kV/m, which was the maximum E-field calculated in the center of the saline solution in section 3.7. For an RF operating frequency of 13.56 MHz, with a period T of 73.7 ns, this would suggest that the US-AuNPs are oscillating back-and-forth across a finite distance of ~0.1 to 0.2 Å within one period of the operating frequency. More so, if the solution is modeled as a perfectly homogenous suspension of US-AuNPs, Equation 6a can be combined with the most general and fundamental form of the Joule heating equation, namely

$$P = IV = \mathcal{N} q v_0(\omega)|E| \quad (7)$$

where P is the power (W), I is the current (A), and V is the voltage. Equation 7 can be directly compared to the SAR (W/Kg) as $\mathcal{N}$ in this instance was calculated for a liter volume of water (where the weight would be equal to 1 kg).

Using Equation 7, the power generated from conversion of electrical energy to thermal energy for 5 nm and 10 nm US-AuNPs (in one second) was found to be between 0.5 - 7.1 W/kg and 0.22 - 3.0 W/kg for 5 nm and 10 nm US-AuNPs respectively, for the E-field range 0.63 kV/m to 2.3 kV/m (previously calculated for a saline sample). Although these values lie below the SAR value calculated previously for the saline solution (1811 W/kg), if the $|E|$ term was squared the values would now be 339 - 16343 W/kg although the units would not reflect those of power. This suggests that there is perhaps another heating mechanism at work which should

4. CONCLUSIONS

The interaction of time-varying RF electric-fields (13.56 MHz) with stable, purified AuNP solutions has been investigated using thermal imaging with complex permittivity and D.C. conductivity analysis. For the range of citrate-capped AuNP diameters studied (5 to 50 nm), only diameters of 10 nm or less exhibited observable heat production (~0.05 to 0.45 oC/s). Hence, we have coined the term “ultra small AuNPs” (US-AuNPs) to differentiate between these RF-active and RF non-active AuNPs. Heat production was also found to depend on both concentration and surface-area and was severely attenuated upon aggregation. These relationships were also confirmed using permittivity and conductivity measurements. Software simulations evaluated the electric-field intensity in-and-around the samples and was shown to range from 90 kV/m in air to 0.63 kV/m - 2.3 kV/m within a saline solution. Although dielectric heat equations could be used to account for the heat response of a saline solution exposed to an RF electric-field exposure in regards to permittivity and electric-field strength, these equations could not account for the greater or equal heating rates exhibited by the US-AuNP samples. Only by modeling dielectric loss as a function of the motion of charged particles in response to a time-varying electric field, as well as power loss as a derivation of the general and fundamental form of the Joule heat equation, could reasonable agreement be realized between experimental and theoretical values. However, a more rigorous theoretical investigation should be undertaken. Our evidence suggests that the heating mechanism most likely originates from the US-AuNPs citrate-surface-coating, the extent of which should be further investigated. Finally, only by creating highly-concentrated, purified, stable suspensions of AuNPs with diameters less than 10 nm, irradiated with high-power RF electric-fields (~90 kV/m) could the heating nature of AuNPs

be observed and analyzed in our experiments, and this is most likely the reason why heating effects have not been observed in previous experimental investigations.[4, 8-9, 11]

Supplementary Material

Refer to Web version on PubMed Central for supplementary material.

Acknowledgments

This work was funded by the NIH (U54CA143837), the NIH M.D. Anderson Cancer Center Support Grants (CA016672), the V Foundation (SAC), The Welch Foundation (C-0627, LJW) and an unrestricted research grant from the Kanzius Research Foundation (SAC, Erie, PA). We thank Kristine Ash from the Department of Surgical Oncology, M.D. Anderson Cancer Center, for administrative assistance.

REFERENCES

1 (a). Lal S, Clare SE, Halas NJ. Nanoshell-Enabled Photothermal Cancer Therapy: Impending Clinical Impact. Account of Chemical Research. 2008; 41(12):1842–1851.(b) Mamiya H, Jeyadevan B. Hyperthermic effects of dissipative structures of magnetic nanoparticles in large alternating magnetic fields. Scientific Reports. 2011; 1(c) Raoof M, Curley SA. Non-invasive radiofrequency-induced targeted hyperthermia for the treatment of hepatocellular carcinoma. International journal of hepatology. 2011; 2011:676957. [PubMed: 21994866]

2 (a). Gannon CJ, Patra CR, Bhattacharya R, Mukherjee P, Curley SA. Intracellular gold nanoparticles enhance non-invasive radiofrequency thermal destruction of human gastrointestinal cancer cells. Journal of nanobiotechnology. 2008; 6:2. [PubMed: 18234109] (b) Gannon CJ, Cherukuri P, Yakobson BI, Cognet L, Kanzius JS, Kittrell C, Weisman RB, Pasquali M, Schmidt HK, Smalley RE, Curley SA. Carbon nanotube-enhanced thermal destruction of cancer cells in a noninvasive radiofrequency field. Cancer. 2007; 110(12):2654–65. [PubMed: 17960610]

3. Moran CH, Wainerdi SW, Cherukuri TK, Kittrell C, Wiley BJ, Nicholas NW, Curley SA, Kanzius JS, Cherukuri P. Size-Dependent Joule Heating of Gold Nanoparticles Using Capacitively Coupled Radiofrequency Fields. Nano Res. 2009; 2:400–405.

4 (a). Hanson GW, Monreal RC, Apell SP. Electromagnetic absorption mechanisms in metal nanospheres: Bulk and surface effects in radiofrequency-terahertz heating of nanoparticles. Journal of Applied Physics. 2011; 109(12):124306.(b) Li D, Jung YS, Tan S, Kim HK, Chory E, Geller DA. Negligible absorption of radiofrequency radiation by colloidal gold nanoparticles. Journal of colloid and interface science. 2011; 358(1):47–53. [PubMed: 21429501]

5. Sassaroli E, Li KCP, O'Neill BE. Radio frequency absorption in gold nanoparticle suspensions: a phenomenological study. Journal of Physics D: Applied Physics. 2012; 45(7):075303.

6. Curley SAC, P. Briggs K, Patra CR, Upton M, Dolson E, Mukherjee PJ. Noninvasive radiofrequency field-induced hyperthermic cytotoxicity in human cancer cells using cetuximab-targeted gold nanoparticles. Journal of Experimental Therapeutics and Oncology. 2008; 7(4):313–326. [PubMed: 19227011]

7. Gach HM, Nair T. Radiofrequency interaction with conductive colloids: permittivity and electrical conductivity of single-wall carbon nanotubes in saline. Bioelectromagnetics. 2010; 31(8):582–8. [PubMed: 20607730]

8. Kruse DE, Stephens DN, Lindfors HA, Ingham ES, Paoli EE, Ferrara KW. A Radio-Frequency Coupling Network for Heating of Citrate-Coated Gold Nanoparticles for Cancer Therapy: Design and Analysis. IEEE Transactions on Biomedical Engineering. 2011; 58(7):10.

9. Liu X, Chen HJ, Chen X, Parini C, Wen D. Low frequency heating of gold nanoparticle dispersions for non-invasive thermal therapies. Nanoscale. 2012

10. Raoof M, Corr SJ, Kaluarachchi WD, Massey KL, Briggs K, Zhu C, Cheney MA, Wilson LJ, Curley SA. Stability of antibody-conjugated gold nanoparticles in the endolysosomal nanoenvironment: implications for noninvasive radiofrequency-based cancer therapy. Nanomedicine. 2012

11. Hanson GW, Patch SK. Optimum electromagnetic heating of nanoparticle thermal contrast agents at rf frequencies. Journal of Applied Physics. 2009; 106(5):054309.

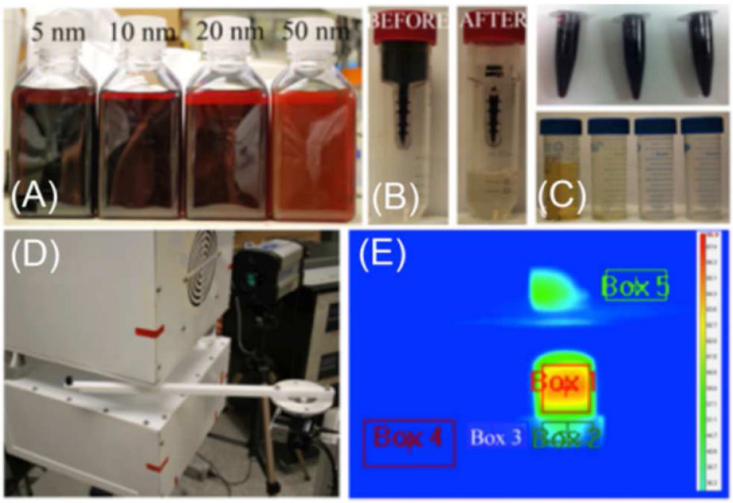

Figure 1.

A) Stock AuNPs of diameter 5 to 50 nm suspended in their buffers (500 ml). B) Solutions were centrifuged through a 50 kDa filter – images shown are before and after centrifugation. C) Filtered AuNPs were concentrated and resuspended in Ω-water (top). Removed buffers are collected and analyzed (bottom). D) Samples were placed on a Teflon sample-holder and rotated into the RF-field. E) An IR camera monitored the temperature changes of the sample (Box 1) and control-areas (Boxes 2 – 5).

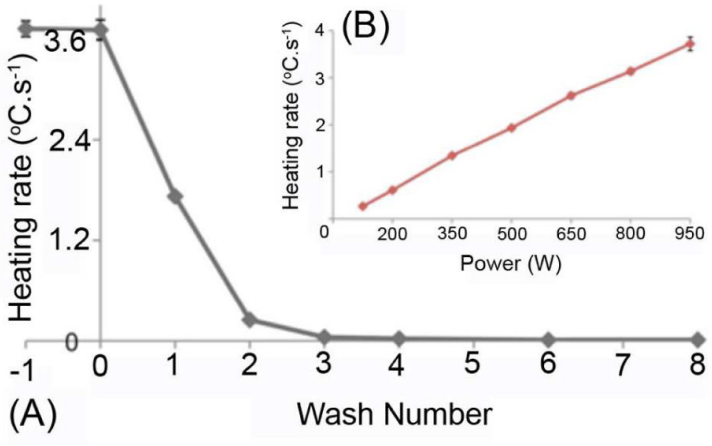

Figure 2.

A) HRs of stock AuNP buffers as a function of wash number. Stock AuNPs (wash # −1) of diameters 5 to 50 nm heat identically to their removed buffers (wash # 0). Eight washes are needed to remove buffers for HRs to be identical to Ω-water (0.01 °C.s^{-1}). B) Heat production for stock AuNPs showed a linear RF power dependent relationship. Data points are combined data for all AuNP diameters.

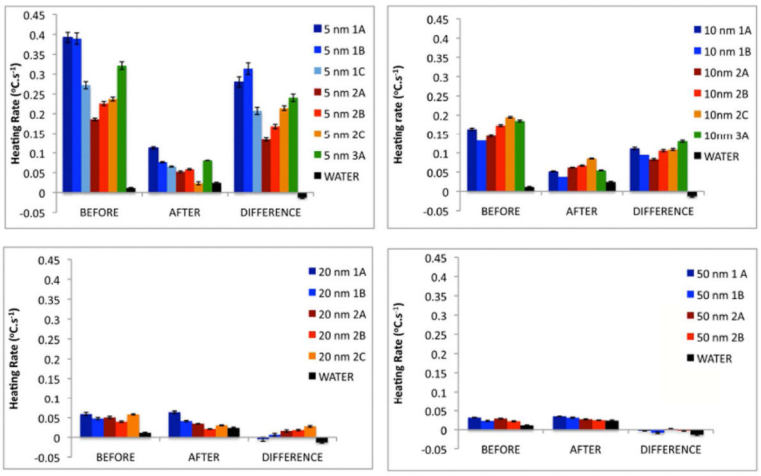

Figure 3.

HRs for AuNPs of diameter 5, 10, 20, and 50 nm. Codes used represent stock bottle number and experimental run (i.e. “10 nm 2B” represents 10 nm AuNPs taken from stock bottle number two, experimental run B). The data depicted in “DIFFERENCE’ represents the HRs due to AuNPs (calculated by subtracting ‘AFTER’ from ‘BEFORE’). Although heating is evident for the 5 nm and 10 nm US-AuNPs, negligible or zero heat was produced for 20 nm and 50 nm AuNPs.

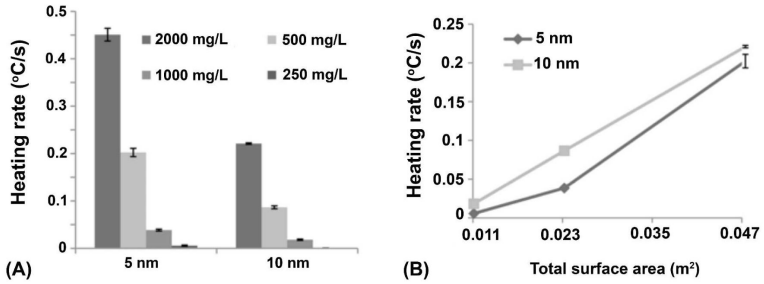

Figure 4.

A) HRs for 5 nm and 10 nm US-AuNPs as a function of Au concentration. Background Ω-water HRs have been subtracted from all US-AuNP HR data. Heating was not observed for AuNPs of diameters 20 nm and 50 nm. B) HRs versus total US-AuNP surface-area in a 1.3 ml sample (for concentrations 500 mg/L to 2000 mg/L). HRs for 5 nm and 10 nm US-AuNPs are approximately equivalent, indicating a strong surface-area relationship to heating.

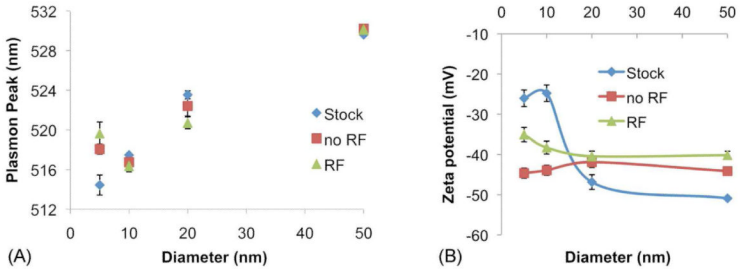

Figure 5.

A) UV-Vis plasmon peak position data for stock AuNP solutions compared to washed AuNPs, before and after exposure to the RF system (no RF and RF, respectively). AuNPs were stable and non-aggregated. B) AuNPs zeta potential measurements: 5 and 10 nm US-AuNPs became more stable, presumably due to removal of excess counter-ions from buffer solutions. 20 and 50 nm AuNPs exhibited a slight loss of surface charge but still gave stable suspensions.

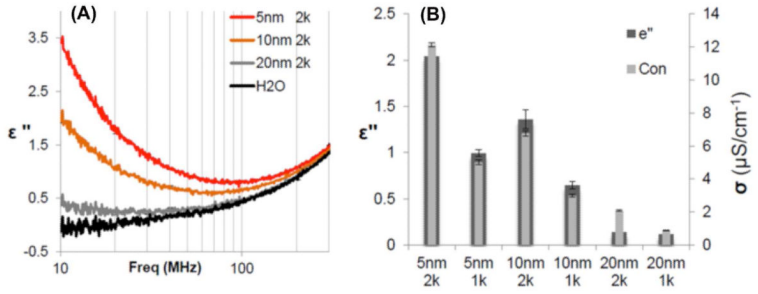

Figure 6.
Permittivity loss (ε”) and D.C. conductivity (σ) data for 5, 10, and 20 nm AuNPs at concentrations of 2000 mg/L.

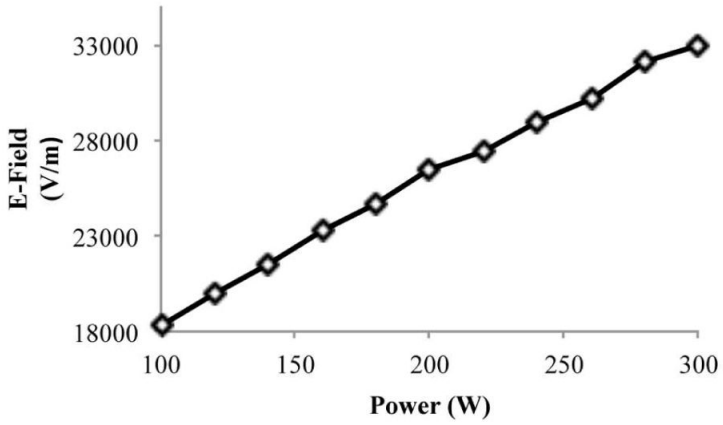

Figure 7.
Measured E-field strength versus RF power.

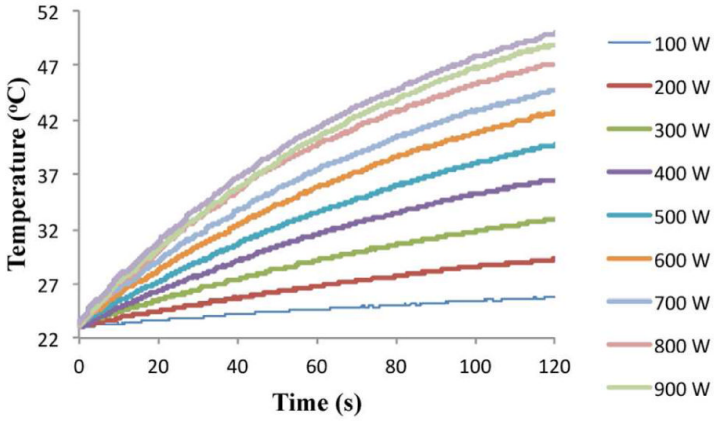

Figure 8.
Temperature versus time plot for saline sample under RF exposure as a function of RF-power.

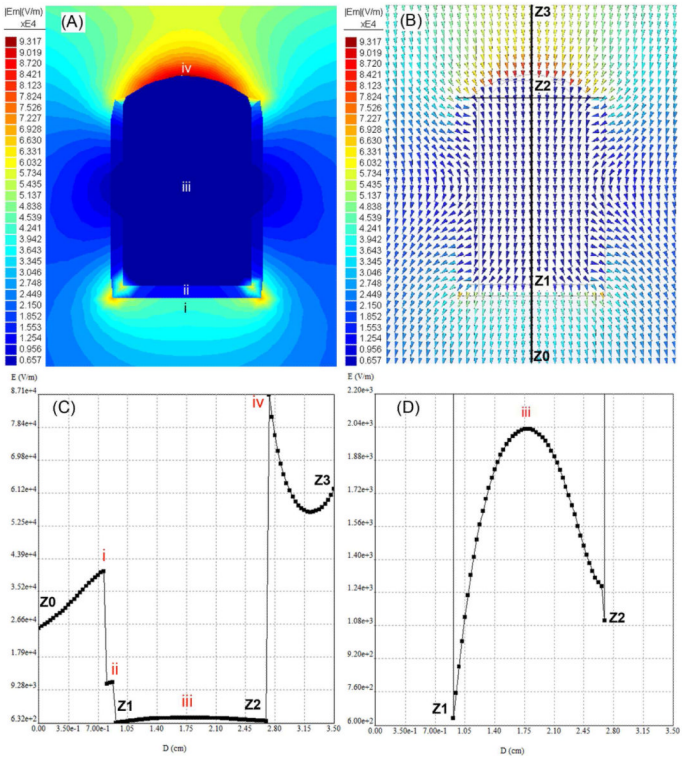

Figure 9.

Simulated electric field lines around a 1.3 ml saline solution suspended in a quartz cuvette. Figure A and B represent electric field contour and arrow vector lines, respectively. A graph of the change of electric field magnitude along a vertical segment from the bottom to the top of the sample (Z0 to Z3) is shown in Figure C (points i to iv in Figure C and points Z0 to Z3 are matched to points i - iv and Z0 - Z3 shown in Figure A and B, respectively). The electric field across the sample itself is magnified in Figure D.

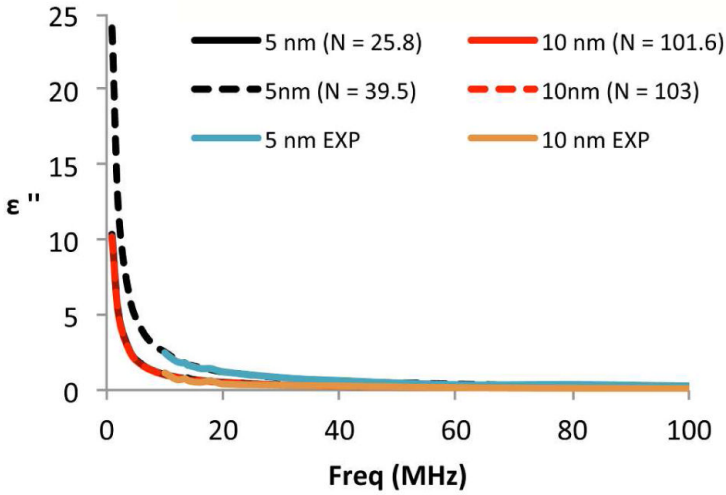

Figure 10.
Dielectric loss for 5 nm and 10 nm solutions for different values of N. The plots of 5 nm (N=25.8), 10 nm (N = 101.6), and 10 nm (N = 103) are similar to each other and lie on the same curve.

Table 1

Simulated E-Field values at differnet interface points (i - iv) and local minima (Z0 - Z3) as seen on Figures 8A and 8B

Interface(s)	E-Field (V/m)	Minima	E-Field (V/m)
i (Air/Quartz)	4.05×10^4	Z0	2.55×10^4
ii (Quartz/Saline)	1.10×10^4	Z1	6.32×10^2
iii (Mid-Saline)	2.3×10^3	Z2	1.1×10^3
iv (Saline/Air)	8.71×10^4	Z3	6.23×10^4

Table 2

Experimental values for HRs of saline and 5 nm/10 nm US-AuNPs are compared to theoretically derived values using Equations 2 and 3. Also shown are the theoretically derived values for SAR

Sample	SAR (W/kg)	HR Theory (°C/s)	HR Experimental (°C/s)
Saline	1811	0.21	0.22
5 nm 2k mg/l US-AuNPs	1.82	2.18×10^{-4}	0.45
10 nm 2k mg/l US-AuNPs	1.24	1.47×10^{-4}	0.22